Evanescent-Wave Filtering in Images Using Remote Terahertz Structured Illumination

M. Flammini,[1] E. Pontecorvo,[2] V. Giliberti,[1,3] C. Rizza,[4,5] A. Ciattoni,[5] M. Ortolani,[1] and E. DelRe[1,6]

[1]*Dipartimento di Fisica, Università di Roma "La Sapienza", 00185 Rome, Italy*
[2]*Crestoptics S.p.A., Via Mattia Battistini 184/D, 00167 Rome, Italy*
[3]*Center for Life Nano Science@Sapienza, Istituto Italiano di Tecnologia, 00161 Rome, Italy*
[4]*Dipartimento di Ingegneria industriale e dell'informazione e di economia, Università di L'Aquila, Via Giovanni Gronchi 18, 67100 L'Aquila, Italy*
[5]*Consiglio Nazionale delle Ricerche, CNR-SPIN, Via Vetoio 10, 67100 L'Aquila, Italy*
[6]*ISC-CNR, Università di Roma "La Sapienza", 00185 Rome, Italy*

(Received 27 February 2017; revised manuscript received 11 September 2017; published 9 November 2017)

Imaging with structured illumination allows for the retrieval of subwavelength features of an object by conversion of evanescent waves into propagating waves. In conditions in which the object plane and the structured-illumination plane do not coincide, this conversion process is subject to progressive filtering of the components with high spatial frequency when the distance between the two planes increases, until the diffraction-limited lateral resolution is restored when the distance exceeds the extension of evanescent waves. We study the progressive filtering of evanescent waves by developing a remote super-resolution terahertz imaging system operating at a wavelength $\lambda = 1.00$ mm, based on a freestanding knife edge and a reflective confocal terahertz microscope. In the images recorded with increasing knife-edge-to-object-plane distance, we observe the transition from a super-resolution of $\lambda/17 \simeq 60$ μm to the diffraction-limited lateral resolution of $\Delta x \simeq \lambda$ expected for our confocal microscope. The extreme nonparaxial conditions are analyzed in detail, exploiting the fact that, in the terahertz frequency range, the knife edge can be positioned at a variable subwavelength distance from the object plane. Electromagnetic simulations of radiation scattering by the knife edge reproduce the experimental super-resolution achieved.

DOI: 10.1103/PhysRevApplied.8.054019

I. INTRODUCTION

According to diffraction theory, monochromatic electromagnetic waves reflected from a material surface form a mixture of propagating and evanescent waves [1]. For propagating waves, the equal-phase and equal-amplitude fronts coincide, whereas evanescent waves display an exponential decay of their amplitude along the propagation axis, so the equal-phase and equal-amplitude fronts are perpendicular. Moreover, evanescent waves transmit no energy and, distinct from their formally analogous exponentially decaying fields in dissipative media such as metals, they occur equally in vacuum and involve no energy dissipation whatsoever. The distinction between propagating and evanescent waves defines the notion of diffraction-limited imaging and super-resolution: a detector placed at a macroscopic distance from an irradiating or reflecting surface will collect only nondecaying propagating waves—i.e., waves that transfer low-resolution details of the image that are typically of the order of the optical wavelength—depending on the numerical aperture of the focusing optics at the object plane (diffraction-limited imaging). In turn, subwavelength spatial details that are encoded in the evanescent waves can be either directly detected using a scanning near-field detector [2] or, in a super-resolution scheme, extracted by processing multiple images using specifically designed excitation-emission techniques with subwavelength spatial modulation, as occurs in structured-illumination imaging [3]. In a standard structured-illumination scheme, the plane at which the illumination is modulated coincides with the object plane to be imaged. Structured illumination can be generalized to conditions in which the two planes do not coincide, as would occur when super-resolution is required for buried objects. In these conditions super-resolution imaging implies a counterintuitive transition from high-resolution to progressively lower-resolution images as the distance of the structured-illumination plane from the object plane increases because high spatial frequencies are progressively lost in the conversion of decaying evanescent waves into propagating ones. While a great variety of microscopy schemes and experiments tap into the evanescent fields, this progressive filtering of the spatial spectrum inherent to remote structured illumination has not been previously experimentally investigated.

Using monochromatic terahertz radiation, we report on the transition from a near-field image, composed of spatial frequencies provided by both propagating and evanescent waves, to a diffraction-limited image, formed only by the spatial spectrum of propagating waves. Using a simple knife-edge scanning scheme, we are able to observe this transition in great detail and quantitatively study the progressive modification of the spectral transfer function as the distance of the knife-edge scanning plane (i.e., the

 © 2017 American Physical Society

structured-illumination plane) from the object plane is increased. The experiment becomes technically possible in the terahertz range because the near-field region extends up to fractions of a millimeter above the sample surface, allowing for mechanical positioning of the knife edge with a precision that is far smaller than the wavelength. In the visible range, the near field extends only a fraction of a micrometer above the sample surface, where surface roughness and electrostatic interactions make positioning with subwavelength precision a challenge.

II. METHODS

A. Fourier analysis

The filtering of high-spatial-frequency components with increasing distance of the structured-illumination plane from the object plane can be mathematically described by considering that an optical field $\mathbf{E}$ of wavelength λ emitted or reflected from a surface obeys the Helmholtz equation $\boldsymbol{\nabla}^2\mathbf{E} + k_0^2\mathbf{E} = 0$, with $|k_0| = 2\pi/\lambda$. This fact implies that each plane-wave component of wave vector $\mathbf{k} = (k_x, k_y, k_z)$ must have $k_x^2 + k_y^2 + k_z^2 = k_0^2$, so if the object plane is taken to coincide with the x-y plane at $z = 0$, the irradiated field can be described in terms of spatial Fourier components as $E = \iint_{-\infty}^{\infty} E(k_x, k_y) e^{(ik_x x + ik_y y)} e^{(i\sqrt{k_0^2 - k_x^2 - k_y^2}\, z)} dk_x dk_y$, where $E(k_x, k_y)$ is the spatial spectrum. Waves with $k_\perp^2 = k_x^2 + k_y^2 \leq (2\pi/\lambda)^2$ leave the object plane in the form of propagating waves. The spatial-frequency components $k_\perp^2 > (2\pi/\lambda)^2$, beyond the so-called Ewald sphere, can be encoded only into evanescent waves that exponentially decay in the z direction as $\exp[-z/z_{\mathrm{ev}}(k_\perp)]$, where $z_{\mathrm{ev}}(k_\perp) = (k_\perp^2 - k_0^2)^{-1/2}$. The consequence is that the field collected by a lens or objective at distances $z \gg \lambda$ contains, at most, details down to the diffraction limit, and subwavelength features with a spatial scale $\Delta x < \lambda$ are inevitably lost [4].

B. Remote super-resolution

The key ingredient in our experiment is the knife-edge scan, which amounts to a super-resolution scheme operating with a structured-illumination plane at a variable subwavelength distance from the reflecting surface where the illuminating radiation is focused (the object plane). The knife-edge scan is a direct embodiment of the basic paradigm of super-resolved imaging: to selectively control the regions of the x-y plane that are allowed to reflect (emit) radiation at a given time, and to acquire multiple images that can then be coanalyzed to extract subwavelength spatial components of the distribution of reflectors (emitters) [5–8]. The knife-edge scan achieves super-resolution in its most basic single-wavelength beam-profiling execution [9,10], in contrast to advanced super-resolution techniques that generally involve radiation delivery and collection at different wavelengths, deconvolution calculations, fluorescence phenomena [11], and/or nonlinear interactions with other light fields [12]. In the terahertz range, knife-edge scans have also been implemented to greatly increase the spatial resolution of images of laser-induced broadband source points, where spatiotemporal aberrations can play an important role [13]. More recently, an optically induced virtual knife-edge technique was also demonstrated by structured illumination with a visible laser of the terahertz-emitting (object) plane [14]. Instead, the transition from near-field imaging to diffraction-limited imaging that we want to investigate here is clear-cut for monochromatic radiation.

To simplify the analysis, let us consider as the object plane a sample surface at $z = 0$ emitting or reflecting radiation in the direction $z > 0$, with subwavelength spatial features that, however, vary only along one of the two transverse directions—say, x. The field intensity distribution at the emitter position is $I(x, z = 0)$. As z increases, the field intensity distribution $I(x, z > 0)$ progressively loses its high-spatial-frequency components with $k_x > 2\pi/\lambda$. An image of the object plane is obtained by reflective confocal scanning microscopy, where the pixels in the image are illuminated one at a time and the corresponding reflected power is separately measured per pixel (details on the experimental setup are given below). Let us now consider a fully opaque blade that scans along the x axis a given plane at a fixed z [see the schematic in Fig. 1(a)]. The intensity distribution immediately after the blade is $O(x, z, x') = I(x, z)\theta(x - x')$, where $\theta(x - x')$ is the step function that represents an ideally sharp blade with its edge in x'; edge-diffraction effects are initially neglected, but they are considered later in the paper. At a distance $z > 0$ from the object plane, the spatial-frequency spectrum of $O(x, z, x')$ is altered compared to that at the object plane $O(x, z = 0, x')$, and it corresponds to the spatial spectrum that can be scattered by the blade in the far field. Scattering of the evanescent-wave intensity by the blade edge into propagating waves newly formed at $z > 0$ allows super-resolved image reconstruction, which is here achieved by subtracting, for each pixel in the image, the total far-field power collected at each blade position x' from that collected at a previous position $x' - dx'$. The intensity distribution reconstructed on the far-field detector is

$$\begin{aligned} I_S(x', z) &= -\frac{d}{dx'} \int_{\mathbb{R}} dx \int_{\mathbb{R}} O(u, z, x')\mathrm{PSF}(x - u) du \\ &= -\int_{\mathbb{R}} I(u, z) \frac{d}{dx'} \theta(u - x') du = I(x', z), \end{aligned} \tag{1}$$

where $\mathrm{PSF}(x)$ is the point-spread function of the light-collecting system [15]. Here, our terahertz reflective scanning confocal microscope has a quasi-Gaussian PSF that is 0.9 mm wide [16]. If the knife-edge scan is carried out on a plane in the near field of the emitting surface, and within the abovementioned ideal blade approximation, the high spatial frequencies of the spectrum of $I(x, z)$ will be fully

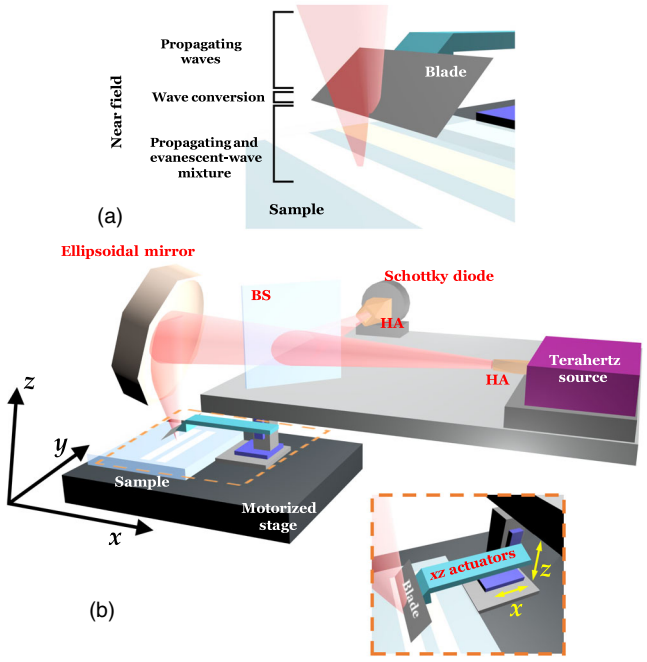

FIG. 1. (a) Knife-edge super-resolution scheme. (b) Terahertz setup. The apparatus is a modified confocal microscope: the radiation at 0.300 THz goes from the source to the sample throughout a quartz beam splitter (BS). The Schottky diode detector is placed at the same distance, 310 mm, from the sample as the source. The ellipsoidal mirror behaves as both focalizing lens and collection lens. Motorized xyz stages allow us to place the sample in the focal plane and make the raster scan. (c) Sketch of the knife-edge profiling system with a steel blade moved by xz actuators. Waveguide-based radiation sources and detectors coupled to the free space using horn antennas (HA) ensure that only light which is focused on the diffraction-limited spot is actually fed into the waveguide [19].

transferred to the reconstructed far-field image $I_S(x,z)$, which is, therefore, no longer limited by diffraction and is a remotely super-resolved image. While Eq. (1) captures the key aspects of our scheme, the ultimate achievable resolution has to be separately evaluated through the rigorous numerical prediction of wave scattering from the blade, as discussed below. Furthermore, our analysis is valid under the assumption that radiation emission by the object is temporally and spatially incoherent, a condition that is here guaranteed by the scanning-confocal-microscopy scheme [17,18].

C. Experimental procedures

We assemble the reflective confocal microscope sketched in Fig. 1(b), similar to the experimental setup of Ref. [16], with an added knife-edge profiling system. The microscope operates at $\lambda = 1.00$ mm ($\nu = 0.300$ THz) with a reflective objective with high numerical aperture (NA $\simeq 0.5$). According to the Rayleigh criterion, the diffraction-limited resolution indicates that two linear image details are resolved if they are more than $\Delta x = \lambda/2$ NA apart in one-directional scans of the sample in the focal spot [16]. The terahertz source is an amplifier-multiplier chain (AMC) from Virginia Diodes. The horn antenna mounted at the end of the AMC emits TEM_{00} radiation with a relative bandwidth $\Delta\lambda/\lambda \simeq 5 \times 10^{-3}$ and constant continuous-wave power of approximately 0.1 mW. The detector is a zero-bias Schottky diode from Virginia Diodes featuring a noise-equivalent power of 1 nW/Hz$^{0.5}$ at a sampling rate of 40 s^{-1}. The fully opaque knife is a steel shaving blade, displaced by a step motor with step precision better than 0.05 μm, much below the typical sampling step size of 10 μm—itself much shorter than λ. The total quartz beam-splitter efficiency is calculated to be about 0.1 at $\lambda = 1.00$ mm [16]. The signal-to-noise ratio is 10^3 per pixel for a totally reflecting sample, while the apparent noise in the images and in the line scans is due to fluctuations in atmospheric absorption and source temperature during the image acquisition, and the noise obviously increases in the super-resolved reconstructions, which require a full set of about 1000 images. The investigated samples are optical lithography masks, made of fused silica coated with a 30-nm-thick chromium film patterned by electron-beam lithography into stripes and squares of different sizes. The root-mean-square edge sharpness is better than 5 nm. The reflectivity of the chromium film in the terahertz range is $R_{Cr} = 0.99$, while the reflectivity of an infinitely thick fused silica plate at normal incidence is $R_{SiO_2} = 0.08$, hence providing strong optical image contrast.

The functioning of the knife-edge super-resolved imaging is conceptually demonstrated by the violation of the Rayleigh principle in the reconstructed images seen in Fig. 2. Therein, the knife-edge scan plane is at a distance $z \simeq 25$ μm $= \lambda/40$, deep into the near field of the object plane. Two parallel stripes at a distance of 230 μm [i.e., the visible-light photography reported in Fig. 2(a)] are imaged. The distance between the stripes lies well below the limit set by the Rayleigh criterion $\Delta x \sim 1$ mm. When no knife-edge scan is implemented, a single broad feature is observed in the confocal microscopy image of Fig. 2(b). The two stripes are too close together and cannot be resolved. In turn, when the knife-edge scan reconstruction is enacted following the recipe of Eq. (1), the two reflecting stripes are clearly distinguished on the nonreflecting background, as reported in Fig. 2(c).

To quantitatively evaluate the imaging resolution reached in the super-resolved reconstruction, we image a sharp border between a chromium surface and a bare silica surface [Fig. 2(d) shows the border using visible light]. The imaging resolution is evaluated by calculating the slope of the line-scan variation from 10% to 90% of the intensity profile of the border. Without the knife-edge technique, we measure a slope of 0.91 mm^{-1} corresponding to an Abbe diffraction limit of 1.1 mm, as shown in Fig. 2(e). In Fig. 2(f), we report the maximum resolution

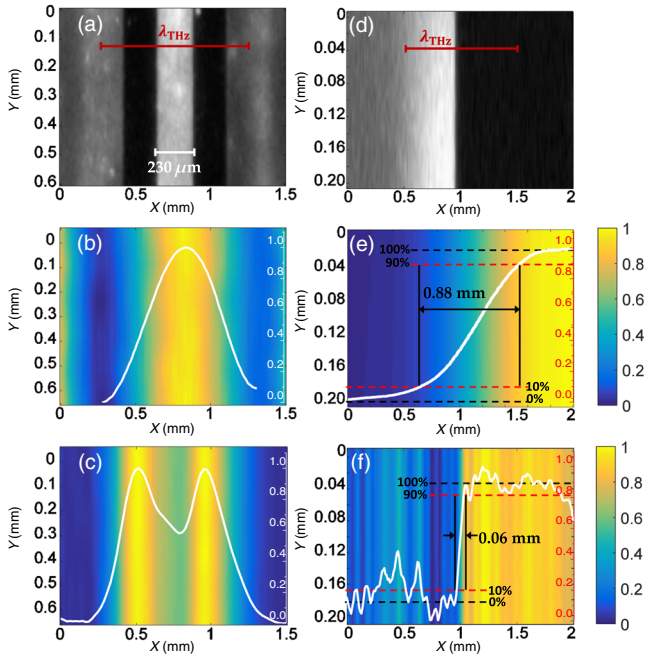

FIG. 2. (a)–(c) Imaging of two chromium stripes on a fused silica substrate, 230 μm $\simeq \lambda/4$ apart. (a) Image taken with visible camera. (b) Image taken with the scanning terahertz ($\lambda = 1$ mm) confocal microscope. (c) Super-resolved image. The two peaks are clearly distinguished. (d)–(f) Imaging of a chromium-silica border. (d) Image taken with a visible camera. (e) Image taken with the scanning terahertz confocal microscope. (f) Super-resolved image with 0.06 mm $\simeq \lambda/17$ line-scan profile width. Images (c) and (f), respectively, are achieved by applying Eq. (1) to 76 images, with one for each 20-μm knife-edge step, and 201 images at 10-μm steps. Profiles and images are in arbitrary units.

achieved using the near-field knife-edge scan. We measure a slope of 13.3 mm^{-1} corresponding to a striking subwavelength resolution of approximately 0.06 mm, or $\lambda/17$. The observed imaging resolution is still 6 times larger than the single step in the confocal microscopy scan of 10 μm, which is chosen as it roughly corresponds to the actual physical sharpness of the blade evaluated with an optical microscope; therefore, a different reason has to be found for the observed imaging resolution on the order of 60 μm. In fact, as discussed below, the imaging resolution is dominated by the spatial width of the edge-diffraction pattern. The finite imaging resolution can be modeled by replacing $\theta(x-x')$ in Eq. (1) by $f_d(x) = \frac{1}{2} + \frac{1}{2}\mathrm{erf}[(x-x')/d]$, where $\mathrm{erf}(x)$ is the error function, so that Eq. (1) can be rewritten as

$$I_S(x,z) = -\int_{\mathbb{R}} I(u,z)\frac{d}{dx'}f_d(u-x')du = \int_{\mathbb{R}} I(u,z)e^{(u-x')^2/d^2}du, \quad (2)$$

where a new convolution integral intervenes and the term $\exp[(u-x')^2/d^2]$ behaves as an effective PSF, and $d \approx 60$ μm quantifies the "effective sharpness" of the blade.

The image in Fig. 2(c) is taken using an x-oriented raster scan. Instead, the images in Figs. 2(f) and 3 are taken with a y-oriented raster scan. The latter raster-scan mode allows one to obtain the most reliable value of the super-resolution because the data along the y direction can be readily integrated before image reconstruction, but it inevitably causes spurious oscillations in the reconstructed image, as the data of adjacent points in the x direction are taken at very different times after one entire y line scan. The multipeak structure appearing around $x = 0.5$ mm in Fig. 2(f) probably has a different physical origin not related to super-resolution imaging, and it is discussed later in this paper.

III. RESULTS

The progressive filtering out of the high-spatial-frequency components from the super-resolved images, caused by the decay of the intensity of the evanescent waves scattered by the blade edge when z is increased, is made evident in Fig. 3. In the top panel, reconstructed line scans similar to those in Fig. 2(f) are shown for several z values. As z increases, one sees the decrease of the slope of the image-intensity step corresponding to the metal-silica border on the sample surface. The lateral (super-)resolution

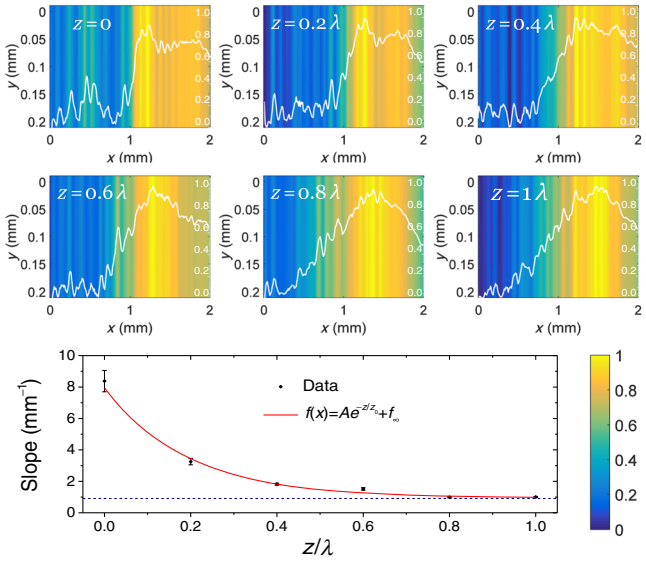

FIG. 3. Transition from near-field imaging to diffraction-limited imaging. (Top panels) As the evanescent-to-propagating wave conversion is performed at $z > 0$, farther from the emitting-reflecting surface, the sharp edge is progressively smeared out (the white line represents the profile). (Bottom panel) The slope of the line-scan profile as a function of z. The points are experimental data, whereas the red line is a guide for the eye represented by the function $f(z) = A\exp(-z/z_0) + f_\infty$, where $A = (7.0 \pm 1.3)$ mm^{-1}, $z_0 = (0.19 \pm 0.03)$ mm and $f_\infty = (0.95 \pm 0.07)$ mm^{-1}. The blue dashed line is $f(z) = 0.91$ mm^{-1}, calculated from the normalized value of the slope of Fig. 2(e) with no knife edge. Profiles and images are in arbitrary units.

can be still defined as the inverse of this slope, and it is reported in the bottom panel of Fig. 3. Interestingly, the slope does not drop to zero for $z \to \lambda$; instead, it tends to the value $f_\infty = 0.91\ \mathrm{mm}^{-1}$ of the standard confocal microscopy image of Fig. 2(e) taken with no blade in the beam path. This asymptotic value of the super-resolution is indicated as a horizontal blue dashed line in the bottom panel of Fig. 3. This fact indicates that, as the intensity of the evanescent waves intercepted by the blade at the given plane z becomes negligible, only the propagating waves are scattered by the blade, and the reconstructed image displays the same lateral resolution as the image without a blade. The red line is an exponential fit to $f(z) = A\exp(-z/z_0) + f_\infty$, which delivers $z_0 = 0.19$ mm; however, as we now explain, a single characteristic exponential decay length for the loss of super-resolution with increasing values of z cannot be defined.

The experimental spatial-frequency spectrum is finally calculated as the one-dimensional Fourier transform of the line scans in Fig. 3 and is plotted in the left panel of Fig. 4. The amplitude decay with increasing values of z is more rapid for the Fourier components at a higher frequency k_x, rather than homogeneously at all k_x values. We emphasize that this phenomenon is not related to energy dissipation, as it occurs without a corresponding attenuation in the total reflected beam intensity, but rather that it is the signature of the progressively reduced capability of the blade edge to scatter the evanescent waves in vacuum towards the far field. As a consequence, the contribution of the evanescent waves to the super-resolved image is progressively filtered out with increasing values of z, and more rapidly for higher k_x values. The experimental spectral filtering can be compared to the theoretical expectation plotted in the right panel of Fig. 4, derived from the Fourier transform of the simplified theoretical line scan of Eq. (2):

$$E(k_x, z) = E(k_x, z=0)e^{i(k_0^2 - k_x^2)^{1/2} z}(k_x < k_0)$$
$$E(k_x, z) = E(k_x, z=0)e^{-(k_x^2 - k_0^2)^{1/2} z}(k_x > k_0). \qquad (3)$$

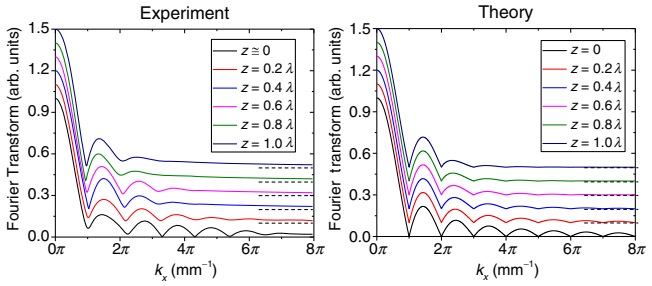

FIG. 4. Filtering of the spatial frequency spectrum in the transition from near-field imaging to diffraction-limited imaging as the distance z between the object plane and the structured-illumination plane increases. (Left panel) Plot of the spectrum displaying a spatial frequency-dependent characteristic decay length, shorter at higher frequencies. (Right panel) The corresponding theoretical prediction obtained exploiting the expressions in Eq. (3).

The main features of the experimental spectra in Fig. 4 are captured by the theoretical model of Eq. (3). As z is increased, there is no single exponential decay length of the image resolution; instead, each k_x component has its own decay length. As z approaches $\lambda/2$, all secondary peaks in the spectra are filtered out, apart from the first one around $k_x \sim 15\ \mathrm{mm}^{-1}$; i.e., only the slowest decaying $k_x \gtrsim 2\pi/\lambda$ values at the edge of the Ewald sphere are still scattered to the far field by the blade. This fact explains the rough validity of the single exponential fit in Fig. 3, with decay length $z_0 = 0.19$, which can be attributed to the lowest spatial-frequency peak at $k_x \sim 15\ \mathrm{mm}^{-1}$, just outside the Ewald sphere. Apparently, this peak alone is sufficient to obtain a super-resolution of $0.5\ \mathrm{mm} \sim \lambda/2$, beyond the diffraction limit $\lambda/2\mathrm{NA} \sim 1$ mm, for a considerable distance of the object plane from the blade scanning plane of $0.4\lambda \sim 400\ \mu$m; i.e., the blade does not need to graze the surface in a terahertz super-resolution microscope.

IV. DISCUSSION

A. Ultimate resolution limit

In order to evaluate the ultimate limit to the super-resolution attained by our technique, we perform a two-dimensional full-wave electromagnetic simulation [20] of the radiation scattering by a metal blade illuminated with a focused Gaussian beam at 0.300 THz. We consider a monochromatic linearly polarized Gaussian beam. The incident field is $\mathbf{E}(x) = \mathrm{Re}[E_0 \exp(-x^2/\sigma^2 - i\omega t)]\mathbf{e}_y$, where E_0 is a constant, $\omega = 2\pi c/\lambda$, and $\sigma = 2\lambda = 2$ mm. The analyzed scattering geometry is shown in Fig. 5(a). The conducting slab representing the blade has a dielectric constant $\epsilon_r = -150 + i50$ and a thickness $L = 40\ \mu$m. We analyze the situation where the incident beam is centered at $x = 0$ and the physical blade edge is at $x = -1.00$ mm, a situation in which the blade should fully obstruct the incident beam, and we monitor the correspondence of the scattered field pattern with the physical position and sharpness of the blade edge. Given the very different length scales involved (λ, z, L) and the presence of metallic surfaces, the simulation is not trivial. The computational domain is terminated with perfect electric-conductor conditions at the $x = \pm 6$ mm planes, and we adopt scattering boundary conditions at the entrance ($z = -17\ \mu$m) and at the exit ($z = 50\ \mu$m) facets of the domain. A suitable discretization of the computational domain is implemented with a maximum and a minimum mesh size of 0.2 mm and 2 μm, respectively (which leads to 125 895 degrees of freedom), and we use the UMFPACK direct solver [20] with default parameters. In Fig. 5(a), we show the z component of the Poynting vector $\mathbf{S}(x, z) = \frac{1}{2}\mathrm{Re}[\mathbf{E} \times \mathbf{H}^*]$. The color plot indicates that, even for an infinitely sharp blade edge, the scattering pattern has a finite dimension and a complex structure, related to well-known edge-diffraction patterns by opaque screens [1].

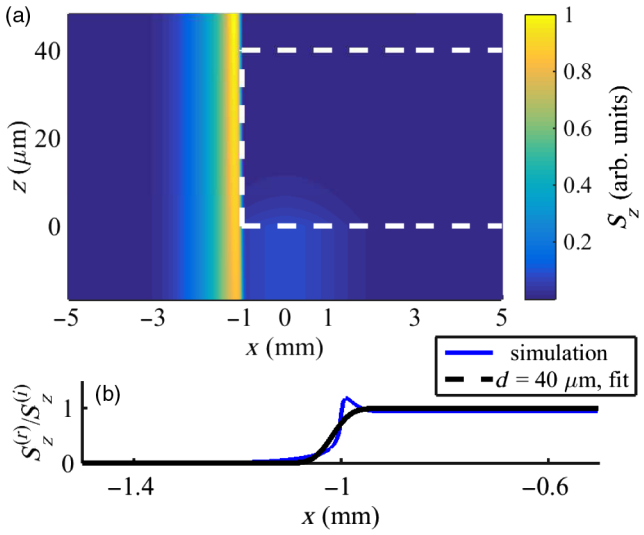

FIG. 5. Numerical electromagnetic simulation of a Gaussian beam with $\nu = 0.300$ THz scattered by a semi-infinite conducting slab of finite thickness $t = 40$ μm. The slab extends in the x-y plane and sits 20 μm from a nonreflecting surface. (a) Image plot of the z component of the Poynting vector $S_z(x, z)$. The dashed white lines are the borders of the slab. Note the very different scale for the z and x axes. (b) Plot of $S_z^{(r)}/S_z^{(i)}$ (the solid line), where $S_z^{(r)}$ and $S_z^{(i)}$ are the z components of the Poynting vector of the reflected and the incident beam at the $z = 0$ plane. The dashed black line is the experimental fit of the function $f_d(x) = \frac{1}{2} + \frac{1}{2}\mathrm{erf}[(x - x')/d]$ for $d = 60$ μm and $x' = -1.02$ mm.

The center of this finite-size field distribution is not at the blade edge (here, $x = -1.02$ mm), but just outside it, at $x' < x$. In Fig. 5(b), we display $S_z^{(r)}/S_z^{(i)}$ (the solid line), where $S_z^{(r)}$ and $S_z^{(i)}$ are the z components of the Poynting vector of the reflected and the incident beam, respectively, at the plane $z = 0$. The ratio $S_z^{(r)}/S_z^{(i)}$ (the blue solid line) represents the effective electromagnetic sharpness of an infinitely sharp blade—and therefore the ultimate limit of our super-resolution scheme. In Fig. 5(b), we superimpose the numerical prediction (the blue curve) with the profile function $f_d(x)$ introduced in Eq. (2) (the black dashed line) with the experimentally determined value $d = 60$ μm and the field-distribution offset $x' = -1.02$ mm. The experimental fit to $f_d(x)$ is done with the least-squares method for x' and fixing $d = 60$ μm from Fig. 2(f). While the offset of 0.02 mm between the reconstructed image and the object is not visible in our experiment, we can conclude from the good superposition of Fig. 5(b) that edge diffraction at the blade termination explains the maximum observed resolution of 60 μm, or $\lambda/17$, well.

Finally, we note that the polarization direction of the electric-field vector can slightly affect the knife-edge reconstruction algorithm [21]; therefore, for comparison, the image in Fig. 2(c) is taken with a polarization parallel to the blade edge (the y axis), while Fig. 2(f) is taken with a polarization orthogonal to it (along the x axis). While the fundamental observation of super-resolution is achieved in both cases, in the latter case, the orthogonal polarization should also excite cavity modes between the metal blade and the metal film on the sample surface. A detailed study of such parasitic proximity effects is beyond the scope of this work, but we speculate that they may be responsible for the multipeak structure seen around $x = 0.5$ mm in Fig. 2(f), where one would instead expect a plateau of very low value of the reconstructed-image pixels. As a partial confirmation of the above, the multipeak structure is already fading away as soon as the blade is lifted from the sample surface at $z \sim 0.2\lambda$, i.e., well below the cutoff distance of evanescent-wave filtering. Therefore, the multipeak structure must be related to near-field oscillations (e.g., surface-plasmon polaritons) whose field extends only in a deeply subwavelength range of z values.

B. Terahertz imaging

From a fundamental perspective, our study provides experimental evidence for the effect of the so-called rigorous diffraction theory on super-resolved terahertz imaging [1]. Here, at the transition between the near-field region and the diffraction-limited wave-propagation region, a mixed regime known as Rayleigh-Sommerfeld diffraction is observed.

The imaging method expands terahertz beam-profiling methods and appears to be fundamentally different from previous imaging techniques since it taps into the full nonparaxial mixture of different spatial Fourier components both inside and outside the Ewald sphere. In a scanning near-field optical microscope [22–26], the tip acts as the equivalent of a δ function in space, capturing and combining the whole spatial spectrum without distinguishing between diffraction-limited and evanescent components, so properties associated with evanescent waves have to be detected by suitable near-field demodulation techniques. Specifically, in a near-field probe experiment, resolution falls off far more rapidly than predicted by Eq. (3), typically at distances from the emitters below $\lambda/6$ (see, for example, Fig. 3 in Ref. [27]).

In order to perform super-resolved terahertz imaging beyond the edge of the Ewald sphere, it is necessary to work at a single wavelength, excluding methods based on wideband excitation where the concept of a diffraction limit is not clear-cut and the highest resolution in the images could potentially be carried by short-wavelength components of the frequency spectrum [28,29].

From a practical point of view, since no subwavelength source or detector is used [30,31], our scheme circumvents the need for a subwavelength aperture, with its crippling many-orders-of-magnitude toll on transmitted power [28,32]; enacts super-resolution with the losses typical of a standard confocal scheme [33]; and does not require ultrasensitive detectors (such as cryogenic bolometers [28]) or high-power sources (such as gas lasers [34,35]).

V. CONCLUSIONS

In this paper, we report on a progressive transition from near-field imaging to diffraction-limited imaging when the structured-illumination plane is lifted from the object plane by distances on the order of one wavelength. The effect is attributed to evanescent-wave-intensity decay, and it is detected using a remote mechanical knife-edge scan technique in a confocal terahertz imaging system. The loss of imaging super-resolution is associated with filtering of the spatial-frequency spectrum of the image, where higher spatial frequencies decay more rapidly with increasing distance and a single exponential decay length cannot be defined for the evanescent-wave intensity. The findings have an immediate impact on the development of super-resolved terahertz imaging, on terahertz imaging of buried structures, and for super-resolution imaging in general in the cases of opaque media and nonplanar emitter surfaces, where the object plane and the structured-illumination plane may not be made to coincide easily.

ACKNOWLEDGMENTS

M. F., M. O., and E. D. acknowledge financial support from the Ricerca di Ateneo Sapienza project and the THESMA Sapienza project. C. R. and A. C. thank the U.S. Army International Technology Center Atlantic for their financial support (Grant No. W911NF-14-1-0315). C. R. thanks CNR-SPIN for the financial support (Seed Project No. B52F17001370005).

[1] M. Born and E. Wolf, *Principles of Optics* (Pergamon Press, New York, 1970), Chap. 11, pp. 556–592.
[2] J.-J. Greffet and R. Carminati, Image formation in near-field optics, Prog. Surf. Sci. **56**, 133 (1997).
[3] F. Ströhl and C. F. Kaminski, Frontiers in structured illumination microscopy, Optica **3**, 667 (2016).
[4] J. W. Goodman, *Introduction to Fourier Optics* (Roberts and Company Publishers, Greenwood Village, CO, 2005).
[5] E. H. Synge, A suggested method for extending microscopic resolution into the ultra-microscopic region, Philos. Mag. **6**, 356 (1928).
[6] E. A. Ash and G. Nicholls, Super-resolution aperture scanning microscope, Nature (London) **237**, 510 (1972).
[7] M. G. L. Gustafsson, Surpassing the lateral resolution limit by a factor of two using structured illumination microscopy, J. Microsc. **198**, 82 (2000).
[8] F. Wei, D. Lu, H. Shen, W. Wan, J. L. Ponsetto, E. Huang, and Z. Liu, Wide field super-resolution surface imaging through plasmonic structured illumination microscopy, Nano Lett. **14**, 4634 (2014).
[9] D. R. Skinner and R. E. Whitcher, Measurement of the radius of a high-power laser beam near the focus of a lens, J. Phys. E **5**, 237 (1972).
[10] A. H. Firester, M. E. Heller, and P. Sheng, Knife-edge scanning measurements of subwavelength focused light beams, Appl. Opt. **16**, 1971 (1977).
[11] E. Betzig, Nobel lecture: Single molecules, cells, and super-resolution optics, Rev. Mod. Phys. **87**, 1153 (2015).
[12] E. DelRe, F. Di Mei, J. Parravicini, G. Parravicini, A. J. Agranat, and C. Conti, Subwavelength anti-diffracting beams propagating over more than 1000 Rayleigh lengths, Nat. Photonics **9**, 228 (2015).
[13] M. Peccianti, M. Clerici, A. Pasquazi, L. Caspani, S. P. Ho, F. Buccheri, A. Jalil, A. Busacca, T. Ozaki, and R. Morandotti, Exact reconstruction of THz sub-λ source features in knife-edge measurements, IEEE J. Sel. Top. Quantum Electron. **19**, 8401211 (2013).
[14] S. P. Ho, A. Mazhorova, M. Shalaby, M. Peccianti, M. Clerici, A. Pasquazi, Y. Ozturk1, J. Ali, and R. Morandotti, Sub-wavelength terahertz beam profiling of a THz source via an all-optical knife-edge technique, Sci. Rep. **5**, 8551 (2015).
[15] C. J. R. Sheppard, Min Gu, and X. Q. Mao, Three-dimensional coherent transfer function in a reflection-mode confocal scanning microscope, Opt. Commun. **81**, 281 (1991).
[16] M. Flammini, C. Bonsi, C. Ciano, V. Giliberti, E. Pontecorvo, P. Italia, E. DelRe, and M. Ortolani, Confocal terahertz imaging of ancient manuscripts, J. Infrared Millimeter Terahertz Waves **38**, 435 (2017).
[17] K. Wicker and R. Heintzmann, Resolving a misconception about structured illumination, Nat. Photonics **8**, 342 (2014).
[18] R. H. Webb, Confocal optical microscopy, Rep. Prog. Phys. **59**, 427 (1996).
[19] A. Kazemipour, M. Hudlicka, R. Dickhoff, M. Salhi, T. Kleine-Ostmann, and T. Schrader, The horn antenna as Gaussian-source in the mm-wave domain, J. Infrared Millimeter Terahertz Waves **35**, 720 (2014).
[20] COMSOL Group, COMSOL MULTIPHYSICS, version 3.4.
[21] C. Huber, S. Orlov, P. Banzer, and G. Leuchs, Corrections to the knife-edge based reconstruction scheme of tightly focused light beams, Opt. Express **21**, 25069 (2013).
[22] O. Mitrofanov, M. Lee, J. W. P. Hsu, I. Brener, R. Harel, J. F. Federici, J. D. Wynn, L. N. Pfeiffer, and K. W. West, Collection-mode near-field imaging with 0.5-THz pulses, IEEE J. Sel. Top. Quantum Electron. **7**, 600 (2001).
[23] A. Apostol and A. Dogariu, Spatial Correlations in the Near Field of Random Media, Phys. Rev. Lett. **91**, 093901 (2003).
[24] R. Mueckstein, C. Graham, C. C. Renaud, A. J. Seeds, J. A. Harrington, and O. Mitrofanov, Imaging and analysis of THz surface plasmon polariton waves with the integrated sub-wavelength aperture probe, J. Infrared Millimeter Terahertz Waves **32**, 1031 (2011).
[25] A. J. Huber, F. Keilmann, J. Wittborn, J. Aizpurua, and R. Hillenbrand, Terahertz near-field nanoscopy of mobile carriers in single semiconductor nanodevices, Nano Lett. **8**, 3766 (2008).
[26] I. C. Moldovan-Doyen, G. Xu, L. Greusard, G. Sevin, E. Strupiechonski, G. Beaudoin, I. Sagnes, S. P. Khanna, E. H. Linfield, A. G. Davies, R. Colombelli, and Y. De Wilde, Low temperature near-field scanning optical microscopy on infrared and terahertz photonic-crystal quantum cascade lasers, Appl. Phys. Lett. **98**, 231112 (2011).
[27] H. Hatano, Y. Inouye, and S. Kawata, Near-field optical microscope with a multiheight scanning, imaging mode, Opt. Lett. **22**, 1532 (1997).

[28] U. Schade, K. Holldack, P. Kuske, G. Wüstefeld, and H.-W. Hübers, THz near-field imaging employing synchrotron radiation, Appl. Phys. Lett. **84**, 1422 (2004).

[29] O. Mitrofanov, M. Lee, J. W. P. Hsu, L. N. Pfeiffer, K. W. West, J. D. Wynn, and J. F. Federici, Terahertz pulse propagation through small apertures, Appl. Phys. Lett. **79**, 907 (2001).

[30] Y. Kawano and K. Ishibashi, An on-chip near-field terahertz probe and detector, Nat. Photonics **2**, 618 (2008).

[31] O. Mitrofanov, T. Tan, P. R. Mark, B. Bowden, and J. A. Harrington, Waveguide mode imaging and dispersion analysis with terahertz near-field microscopy, Appl. Phys. Lett. **94**, 171104 (2009).

[32] A. J. Macfaden, J. L. Reno, I. Brener, and O. Mitrofanov, 3 μm aperture probes for near-field terahertz transmission microscopy, Appl. Phys. Lett. **104**, 011110 (2014).

[33] N. Karpowicz, H. Zhong, C. Zhang, K.-I. Lin, J.-S. Hwang, J. Xu, and X.-C. Zhang, Compact continuous-wave subterahertz system for inspection applications, Appl. Phys. Lett. **86**, 054105 (2005).

[34] M. A. Salhi, I. Pupeza, and M. Koch, Confocal THz laser microscope, J. Infrared Millimeter Terahertz Waves **31**, 358 (2010).

[35] S. Mair, B. Gompf, and M. Dressel, Spatial and spectral behavior of the optical near field studied by a terahertz near-field spectrometer, Appl. Phys. Lett. **84**, 1219 (2004).